On the global estimates of geostrophic and Ekman surface currents

Joel Sudre, Christophe Maes, Veronique Garçon

Limnology and Oceanography
FLUIDS & ENVIRONMENTS

ORIGINAL ARTICLE

On the global estimates of geostrophic and Ekman surface currents

Joël Sudre,[1] **Christophe Maes,**[2] **and Véronique Garçon**[1]

Abstract

Surface currents in oceanic environments are of crucial importance because they transport momentum, heat, salt, and tracers over large distances that regulate both the local and large-scale climate conditions, and because they contribute to the Lagrangian displacement of floating material, ranging from living resources to marine pollution. In recent decades, the understanding of surface currents has benefited from the opportunity of observing sea level and wind stress via satellite-derived measurements. Combining these parameters into geostrophic and wind-driven components provides an estimate of surface currents with a quarter-degree horizontal resolution at a global scale and at a daily time scale. In the present study, improvements are made on the consideration of the time dependence of the main parameters implied in the determination of the Ekman wind-driven component, and on the treatment of the equatorial singularity. The resulting Geostrophic and Ekman Current Observatory (GEKCO) estimates were validated with independent observations from both Lagrangian and Eulerian perspectives. The statistics of comparison were significant over the globe for the 2000–2008 period. The only exception was the estimation of meridional current along the equator, which requires further developments of the dynamic model and, probably, more accurate measurements. Applications using our GEKCO surface current estimates in cross-disciplinary approaches from physical oceanography to marine ecology are presented and discussed.

Keywords: drifter buoys, Lagrangian trajectory applications, ocean circulation and dynamics, physical oceanography

Introduction

[1] Before the modern era of satellite observation, ocean surface currents were mainly estimated using data from historical ship drift (Richardson 1989). Since 1978, satellite-tracked drifters (issued from the National Oceanic and Atmospheric Administration's Atlantic Oceanographic and Meteorological Laboratory [AOML] Surface Velocity Program, now known as the Global Drifter Program) have been deployed in all ocean basins and have allowed computation of oceanic currents at global scales (Niiler et al. 2003; Lumpkin and Pazos 2007). These efforts take a long time to sample the global ocean in order to estimate the mean climatology of surface currents; furthermore, the analysis of variability remains problematic due to the coarse spatiotemporal sampling, which leaves some regions largely unexplored (e.g., Arctic and Antarctic). Moreover some key regions, such as equatorial divergence areas, are mostly undersampled because of the nature of

[1]CNRS/LEGOS, 18 av. E. Belin, 31401 Toulouse Cedex 9, France

[2]IRD/LEGOS, 18 av. E. Belin, 31401 Toulouse Cedex 9, France

Correspondence to Joël Sudre, joel.sudre@legos.obs-mip.fr

surface drifters. Repeated satellite observations of sea level offer the opportunity to study mesoscale eddies through the geostrophic approximation over the ocean (Chelton et al. 2011). Combined with wind stress fields also observed from space, ocean surface circulation can be determined by a steady balance between geostrophic and Ekman dynamics (Lagerloef et al. 1999).

[2] The transport of heat and freshwater by ocean currents is crucial in climate variability and varies at both regional and global scales. In the Pacific Ocean, the zonal displacement of the western Pacific warm pool has strong implications in ocean atmosphere interactions associated with El Niño/Southern Oscillation (ENSO) at the interannual time scale (Picaut et al. 1996). The horizontal convergence of currents at the eastern edge of the warm pool results in a front of surface salinity (Maes et al. 2006) and a significant chlorophyll *a* gradient that is accurately monitored by satellite remote sensing (Maes et al. 2010). Surface current anomalies can lead ENSO or sea-surface temperature anomalies by a few months, representing a potential way to predict the arrival of the warming conditions in the eastern Pacific associated with ENSO (Lagerloef et al. 2003). At seasonal time scales, the mean surface divergence also links the equatorial band to the subtropical dynamic a few years later as part of the subtropical cells (Johnson 2001).

[3] In the euphotic zone, the surface currents associated with mesoscale structures strongly influence ocean biogeochemistry via advection, lateral stirring, frontal instabilities, and eddy pumping (Garçon et al. 2001). The latter process supplies nutrients to the upper layers and thus fuels phytoplankton growth and the subsequent marine food chain. The relationship between the ocean dynamics and biogeochemical variability is rather complex and not fully understood. For instance, the Agulhas current sustains long-lived and intense bloom events in the subtropical convergence zone south of Africa (Llido et al. 2005). By contrast, in the four major eastern boundary upwelling systems, the horizontal mixing counteracts the nutrient Ekman pumping, which remains nevertheless the dominant process (Rossi et al. 2008). Over the oceans, physical processes influence plankton dynamics (Abraham 1998) up to the ecology of the marine megafauna (Tew Kai et al. 2009; Robel et al. 2011).

[4] Quantifying ocean currents at global scale with a high level of accuracy is of significant cross-disciplinary interest. This relates to the aforementioned role of ocean currents as an initiator and moderator of climate variability and the influence on biological properties, including the behavior of marine animals. Whereas a number of approaches offer a comprehensive view of ocean motion at unprecedented spatial and temporal scales (e.g., Dohan and Maximenko 2010), they also include several discrepancies (e.g., amplitude of the mean current along the equator and the variability of meridional current within the tropical band, especially at the frequency of the tropical instability waves; Johnson et al. 2007; Sudre and Morrow 2008). The aim of this study is to improve estimates of the wind-driven currents via standard Ekman formalism and to tackle the specific singularity of the equator. The proposed Geostrophic and Ekman Current Observatory (GEKCO) is described methodologically, along with the different data sets required. The results presented include a broad overview of the mean and variability of the currents and a cross-validation using independent data sets. The implications of these results for ocean dynamics and cross-disciplinary applications are discussed.

Methods

[5] Oceanic currents result from movements of fluid particles in response to internal forces (pressure gradients and Coriolis forces), external forces (gravity force), and frictional forces (dominated in the surface ocean by wind stress). Steady ocean currents derive from balances between these different forces. A primary balance is between the horizontal pressure gradient and the Coriolis force, resulting in "geostrophic flow." Historically, the surface geostrophic flow was deduced by in situ observations of the geopotential anomaly determined from density profiles (resulting from temperature and salinity data). At the surface, it is also necessary to account for the wind-driven currents (or Ekman currents) that result from the balance between the frictional stress due to the wind and the Coriolis force. Theoretically,

the wind-driven component of mass transport in the surface (Ekman) layer is perpendicular to the mean wind stress, to the left of the wind stress in the southern hemisphere and to the right in the northern one. At the surface, the current associated with this transport deviates from the wind direction by 45°, and the amplitude decreases down to the Ekman layer depth following a spiral. In the tropical Pacific, Ralph and Niiler (1999) highlighted that 78% of the variance of ocean current as observed by Lagrangian drifters drogued at 15-m depth could be explained by the geostrophic and Ekman currents (63% and 15%, respectively). This important result provides the basis for estimating ocean surface currents at global scale computed from satellite altimetry and surface vector winds. In the following, we define zonal and meridional currents (u, v) as the sum of geostrophic (u_g, v_g) and Ekman (u_e, v_e) components. A user-friendly program for computing the oceanic currents at specified worldwide locations is available from the authors (www.legos.obs-mip.fr/sudre/mesoscale-oceanic-current-extracting-program).

The Geostrophic Component

[6] The geostrophic balance assumes that momentum advection and frictional forces are small. Outside the equatorial band (where the Coriolis force vanishes), geostrophic velocities are given by

$$u_g = -\frac{g}{f}\frac{\partial h}{\partial y} \tag{1a}$$

and

$$v_g = \frac{g}{f}\frac{\partial h}{\partial x}, \tag{1b}$$

where y and x are the latitude and longitude positions, f is the Coriolis parameter, g is the acceleration due to gravity (9.807 m s^{-2}), and h is the map of absolute dynamic topography (MADT) that results from the elevation of the sea surface height referenced by the geoid. The latter field represents the product from the Data Unification and Altimeter Combination System available on the AVISO (Archiving, Validation and Interpretation of Satellite Oceanographic data) website (www.aviso.oceanobs.com/en/data/productsinformation/duacs). This product provides a daily and global projection onto a Mercator grid (resolution of 1/3°). Our geostrophic component based on Eqs. 1a and 1b are determined on a regular grid at 1/4° resolution using bilinear interpolation.

[7] Eqs. 1a and 1b are singular at the equator, where $f = 0$, and are problematic nearby because the Coriolis force is small. However, both equatorial theory and several studies based on observations (Moore and Philander 1978) suggest the use of the second derivative of the meridional pressure field on an equatorial β-plane ($f = \beta y$, where β is a constant). When applied to the MADT, the equations for each component of the so-called "semigeostrophic" current (u_{sg}, v_{sg}) become

$$u_{sg} = -\frac{g}{\beta}\frac{\partial^2 h}{\partial y^2} \tag{2a}$$

and

$$v_{sg} = \frac{g}{\beta}\frac{\partial^2 h}{\partial x^2}, \tag{2b}$$

where $\beta = 2.3 \times 10^{-11}$ m^{-1}s^{-1}. A condition to use Eqs. 2a and 2b at the equator is that the first meridional derivative of h needs to be null. A correction factor is then introduced to the MADT in order to force that condition, following the procedure detailed by Picaut and Tournier (1991). Away from the equator, the continuity between Eqs. 1a and 2a (Eqs. 1b and 2b, respectively) is ensured by applying a classical spline function within the 2°N–2°S band. Outside of this band, the estimates of current remain purely geostrophic.

The Ekman Component

[8] The Ekman regression model of the wind-driven current, following van Meurs and Niiler (1997) and Lagerloef et al. (1999), represents the following linear steady momentum balance,

$$fh_e u_e + r_e v_e = \tau_y/\rho \tag{3a}$$

and

$$r_e u_e - fh_e v_e = \tau_x/\rho, \tag{3b}$$

where $\tau(\tau_x, \tau_y)$ is the wind stress field, $\rho = 1025$ kg m^{-3} is the water density, and h_e and r_e are, respectively, the thickness of the Ekman layer and the linear drag coeffi-

cient that represents the vertical viscosity terms as a body force on the Ekman components. These latter parameters need to be determined before estimating the Ekman current, but they are largely unknown for the real ocean. For instance, Lagerloef et al. (1999) derived (h_e, r_e) based on an empirical multiple linear regression using the Lagrangian surface drifters, but these parameters were constant spatially and temporally. Extending this approach from the Pacific to other basins, Sudre and Morrow (2008) pointed out that improvement for the Ekman component was needed to account for the strong variability of the Ekman layer. This is a very complex problem that could be addressed, pragmatically, by estimating (h_e, r_e) from observations. Indeed, once the geostrophic component has been removed from the current observed by surface drifters, the residual is assumed to represent the Ekman current. Based on the equilibrium as stated by Eq. 3a and 3b, the (h_e, r_e) parameters could be expressed as

$$h_e = \frac{1}{f}\frac{\tau_y u_e - \tau_x v_e}{\rho\left(u_e^2 + v_e^2\right)} \tag{4a}$$

and

$$r_e = \frac{\tau_x u_e + \tau_y v_e}{\rho\left(u_e^2 + v_e^2\right)}. \tag{4b}$$

In the next step, we determined linear regressions between (h_e, r_e) and the wind stress modulus regionally over the global ocean, and we used these slopes to estimate u_e and v_e through Eqs. 3a and 3b. To avoid discontinuity and to treat regions poorly sampled by surface drifters, we kept only the latitude dependence of these relationships when they are averaged by basin. Fig. 1 illustrates how the complete methodology applies: for each parameter, the value was determined by considering the input of observed wind stress (Fig. 1A) and the climatological slope based on the aforementioned linear regression (Fig. 1B, C, respectively, for h_e and r_e). The resulting thickness of the Ekman layer and linear drag coefficient are displayed per basin on Fig. 1, D and E. In the Pacific and Atlantic, the equatorial Ekman layers reach values $\sim$30 m, which is well known in these regions. Outside of the equatorial band, values decrease to $<$10 m toward polar regions.

Ancillary Data

[9] To evaluate the Ekman current, we used the mean wind field data from the ku-band microwave scatterometer (SeaWinds) onboard the *QuikSCAT* satellite, distributed by the Centre ERS d'Archivage et de Traitement (CERSAT). The global daily product at 1/2° resolution is processed by a bilinear interpolation on a 1/4° regular grid and is available from 19 July 1999 to 21 November 2009.

[10] To evaluate the Ekman layer depth and the drag coefficient, we used a set of 6951 drifters drogued at 15-m depth over the global ocean during the period from 18 July 1999 to 31 March 2009 from the Global Drifter Program at AOML. To obtain the drifter velocity, we first smoothed the positions over a 72-h window to filter the inertial movements from drifter displacements. Second, the speed and direction (referenced to the north) of each drifter were calculated at each point considering two consecutive positions at six hourly intervals.

[11] To validate the time variability with independent data, we used direct observations of equatorial currents by Acoustic Doppler Current Profiler (ADCP) moorings at several discrete locations within the Pacific, Atlantic, and Indian oceans known as the TAO/TRITON, PIRATA, and RAMA arrays, respectively. Due to the backscatter from the ocean surface in the upper 30–40 m, additional current meters were included in some moorings near the surface. In the following, we used both types of observation independently as soon as observations were available at the minimum depth of 25 m in order to validate our surface currents. Only the data qualified as good or probably good (meaning that pre/post deployment calibrations have been applied) were considered hereafter.

[12] Two other sources of independent data of surface current were provided by hull-mounted ADCP and by the estimates of surface drifting in Argo floats. These data sets are very different, the former providing estimates of the horizontal current at a depth range of between 20 and 300 m every $\sim$5 min, whereas the latter

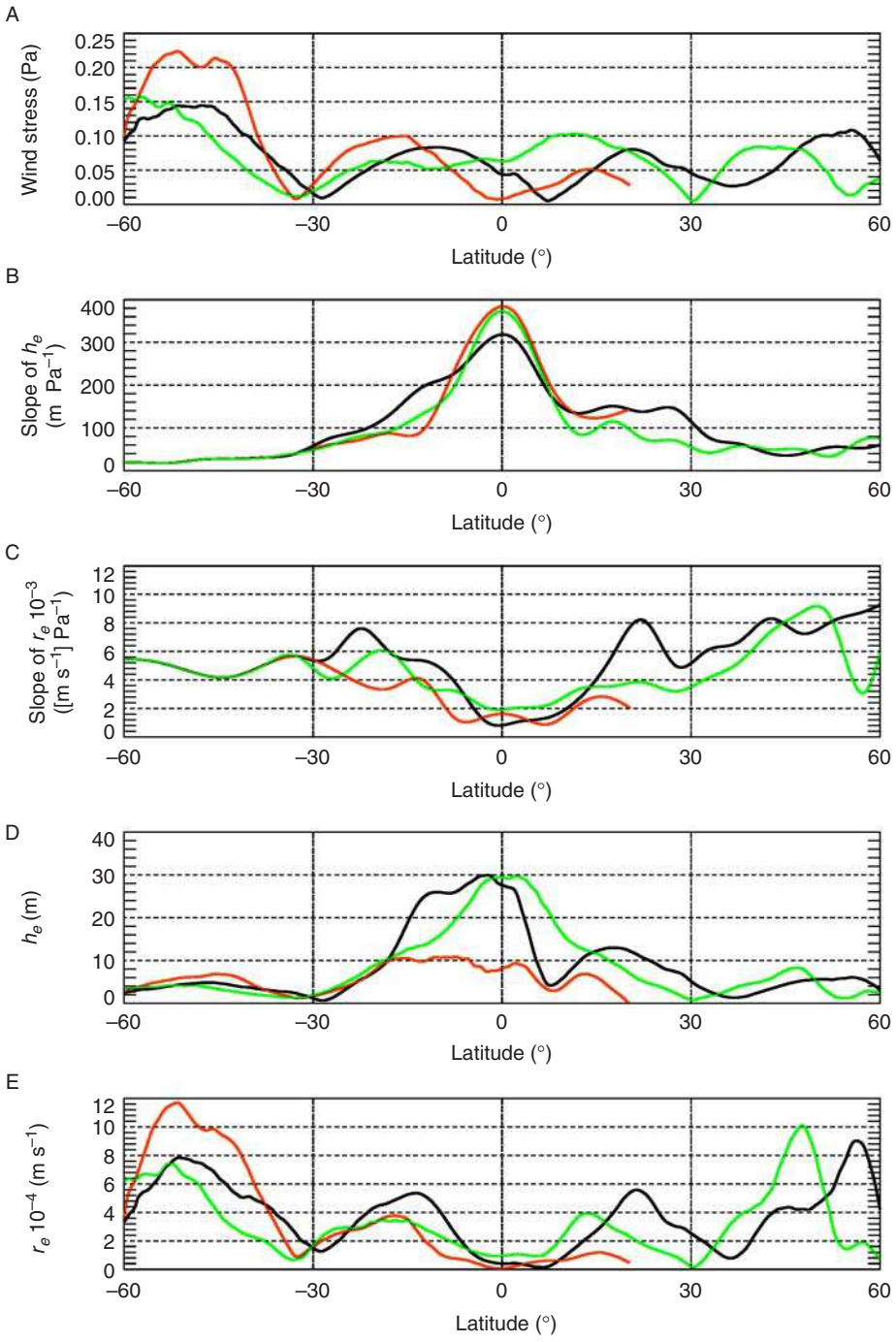

Fig. 1 Meridional section of wind stress (A), slope of the thickness of the Ekman layer (h_e) (B), slope of the linear drag coefficient (r_e) (C), and h_e and r_e per basin (D and E, respectively). Red, green, and black lines indicate Indian, Pacific, and Atlantic basins, respectively.

relies on the evaluation of surface current from the displacement of the float during the time at the surface required for satellite communication each ~10 d cycle. The ADCP current at the 20-m depth (qualified as good data only), represented 265 cruises operated on research vessels between 21 July 1999 and 22 July 2009 from the Joint Archive for Shipboard ADCP (Hummon and Firing 2003). Since the 2000s, the emergence of the Argo program offers a unique data set with global coverage that represents an alternative to the traditional drifters. We used the estimates analyzed and distributed by Xie and Zhu (2008, 2009) over the period 2000–2008. Each current evaluation based on Argo floats is considered an independent datum, and the GEKCO estimates were determined by considering the mean current between the initial and the final positions of the Argo float during its surface time. Furthermore, the geographical deployment of the Argo floats offers a complementary view for several regions that remain poorly sampled, and the error estimate in surface currents ($<5\,\mathrm{cm\,s^{-1}}$) is equivalent to the accuracy of surface drifters (Xie and Zhu 2009). In order to provide statistics comparable with those from the drifters, the data and statistics were compiled with a global repartition by $5° \times 5°$ bins.

[13] Different references for the climatology of mean currents were also considered. The drifter-derived climatology is based on the analysis described by Lumpkin and Garraffo (2005)

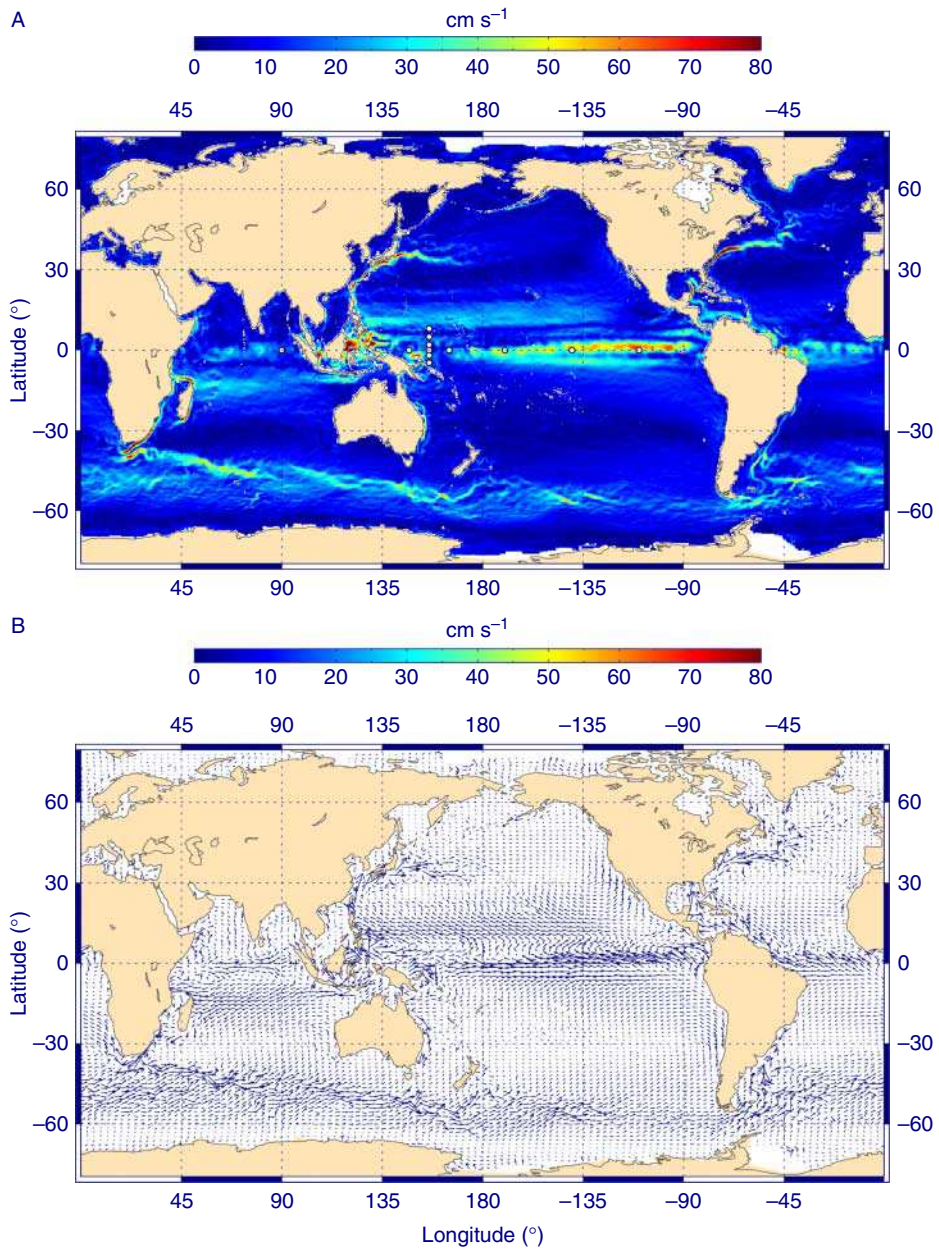

Fig. 2 Amplitude (A) and vector representation (B) of the total surface current (in cm s^{-1}) averaged for the 2000–2008 period and based on the present combination of geostrophic and wind-driven estimates. The white dots on the first panel mark the positions of the TAO/TRITON moorings.

in which the final global results were smoothed via optimum interpolation assuming a Gaussian autocorrelation function with an isotropic e-folding scale of 150 km. More locally, meridional sections of ADCP shipboard zonal mean currents were compiled by Johnson et al. (2002) in the Pacific, primarily during the 1990s. In the Atlantic Ocean, we considered the section of zonal current at 18-m depth and along 10°W as described in the compilation of 18 cross-equatorial shipboard current profiling sections by Kolodziejczyk et al. (2009).

Results

[14] To understand the role of the ocean dynamics, the currents supplying and transporting heat, freshwater and biogeochemical properties need to be thoroughly investigated. The scope of the present paper is to offer a global survey of the major ocean currents rather than to describe the details of the different regional aspects of the surface circulation. As mentioned previously the near-surface circulation is driven primarily by the wind stress and forced into closed circulation cells by the continental boundaries. The main features that emerge from the annual mean circulation (Fig. 2) pertain to the strength of the tropical circulations, especially in the Atlantic and Pacific oceans, which share features because of the prevailing trade winds. The expected intensified currents near the western boundary are the Gulf Stream and the Kuroshio currents in the northern hemisphere of the Atlantic and Pacific oceans, respectively, but they also include the Brazil-Malvinas confluence region and the East Australian Current in the southern hemisphere. Around the

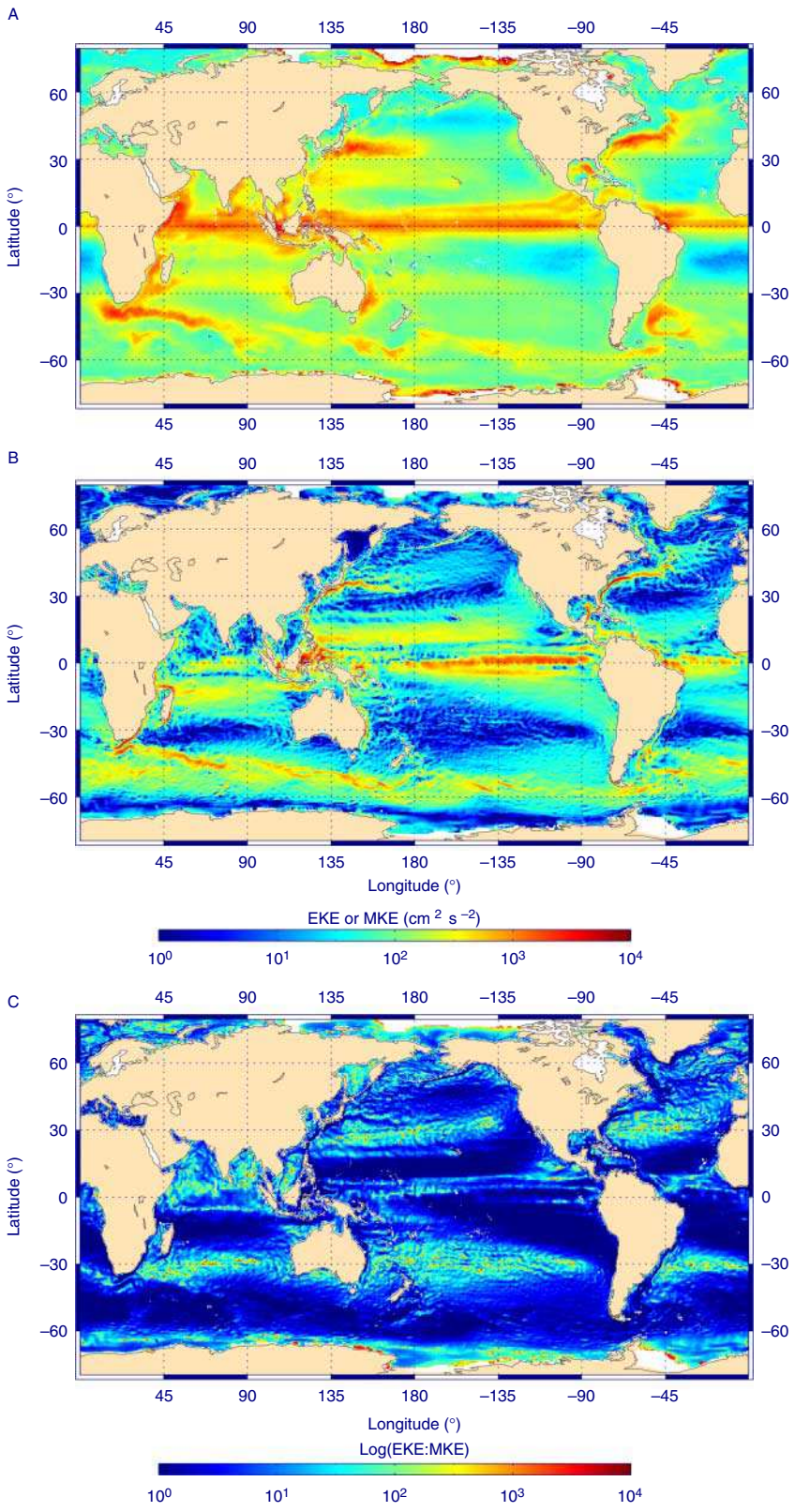

Fig. 3 Time-mean average of the eddy kinetic energy (EKE, in $cm^2\ s^{-2}$; A), mean kinetic energy (MKE, in $cm^2\ s^{-2}$; B), and EKE:MKE ratio (C). All the fields are plotted with the same logarithmic scale.

Antarctic continent, the Antarctic Circumpolar Current (ACC) provides the most significant interocean conduit by which waters of the three major basins interact. Rather than a broad flow, the ACC is composed of a number of high-energy jets separated by zones of weak currents, or even reversed westward flow. In the southern tip of Africa, the Agulhas current system that forms the western boundary system of the South Indian Ocean lies between the ACC and the subtropical convergence zone (near 40°S). The most prominent feature of this system is the retroflection of the Agulhas current in a tight loop with eastward flow as a return current (Fig. 2B). The high variability in the mesoscale activity resulting from this unstable loop configuration is important not only for the circulation in the Indian sector but also for the exchange of properties carried by the different eddies that detach and drift northward into the South Atlantic Ocean.

[15] The mean currents, as well as their variability, are of importance for energy transfer processes related to the general ocean circulation. In the ocean, the mesoscale activity lies roughly on spatial scales of 30–1000 km and time scales of 10–300 days. The eddy kinetic energy (EKE) is well suited to map this variability and can be defined by

$$\mathrm{EKE} = \frac{1}{2}(u'^2 + v'^2), \qquad (5)$$

where u' and v' are the velocity anomalies defined as the difference of current with the annual mean currents $(\bar{u}, \bar{v})$, as shown in Fig. 2A. Fig. 3A shows the averaged EKE

during the 2000–2008 period. The highest values ($>3000\,\mathrm{cm^2\,s^{-2}}$) were typically found along the equatorial band and the extension of the major western boundary currents. The reversal twice a year of the Somali current due to the monsoon is responsible for the strong EKE in the western North Indian Ocean. Another pronounced high variability area is associated with the path of the ACC and is related to the meandering structures, including the Agulhas retroflection. Weaker peaks in EKE were observed in the subtropical region in each basin. Many local structures could be identified with specific dynamic regimes such as the loop current in the Gulf of Mexico, the north equatorial retroflection in the equatorial western Atlantic, and the pathway of south equatorial current around the southern part of Madagascar and into the Mozambique Channel.

[16] The relationship of EKE to large ocean circulation (which feeds EKE by barotropic and baroclinic instability) may be probed by examining the distribution of mean kinetic energy (MKE), defined as

$$\mathrm{MKE} = \frac{1}{2}(\bar{u}^2 + \bar{v}^2). \tag{6}$$

Similarly to EKE, values of MKE (Fig. 3B) exhibited maxima $> 3000\,\mathrm{cm^2\,s^{-2}}$ in the major western boundary current regions, the ACC, and the tropics. However, these structures were thin, a result that is consistent with the idea that EKE is generated in areas of strong shear in mean flow. The ratio of EKE:MKE (Fig. 3C) shows areas where the ocean dynamics were stable (the ratio ranges between 1 and 10), as well as more turbulent (areas where this ratio exceeds 100). The former includes the pathway of the major western boundary currents, where the reduced EKE:MKE ratio is aligned along regions of enhanced MKE (Fig. 3B). It also includes the Labrador Current, the Alaskan stream flowing along the Aleutian Islands, the East Kamchatka Current, and the Norwegian Atlantic Current with its coastal extension. The five regions of high EKE:MKE values are approximately centered around 30° in the subtropics and cover each entire basin from east to west. In most of these areas, a ratio >1000 was found. High values of EKE:MKE were also found at regional scale such as the Bay of Bengal, Arabian Sea, South China Sea, Okhotsk Sea, and the Nordic Seas.

[17] The comprehensive global coverage of ocean currents in both space and time is an advantage inherent to satellite-derived fields, which also makes exhaustive validation with independent observations challenging. We used ADCP current meters, either hull mounted on ships or fixed on anchored mooring at different ocean sites, and estimates of currents derived from surface displacement of Argo floats. Each data set is characterized by heterogeneous samplings, both in time and in space, reflecting in part the dichotomous nature between their Lagrangian versus Eulerian dimension. Table 1 presents the statistics for zonal and meridional components in the three tropical regions where hull-mounted ADCP data density is reasonable. Similar standard deviations were found between in situ observations and GEKCO values in all regions. Not surprisingly, lower correlations characterized the meridional component (~0.5) compared with the zonal ones (~0.7), but both correlations were statistically significant. In order to focus on the variability, we used the

Table 1 A — Comparisons for the zonal component (u) between the data observed by shipboard ADCP and the GEKCO model estimates. N represents the number of collocated points to evaluate the mean, standard deviation (SD), root mean square difference (RMS dif), and correlation ($p > 95\%$ level of confidence). B — Same comparisons for the meridional component (v). The separation between the western and eastern parts of the Pacific (WPAC and EPAC, respectively) is located at 155°W. ATL, Atlantic basin.

A	u	N	Mean	SD	RMS dif	Correlation
WPAC	ADCP	5021	−4.46	29.87	23.37	0.70
	GEKCO		−8.73	29.42		
EPAC	ADCP	6915	−9.46	35.62	26.55	0.73
	GEKCO		−17.49	33.15		
ATL	ADCP	1636	−6.36	25.45	20.28	0.67
	GEKCO		−7.66	24.01		
B	v	N	Mean	SD	RMS dif	Correlation
WPAC	ADCP	5021	−0.26	19.12	18.72	0.45
	GEKCO		−0.43	16.18		
EPAC	ADCP	6915	−1.13	25.86	23.42	0.50
	GEKCO		4.09	17.20		
ATL	ADCP	1636	−3.38	23.97	22.22	0.46
	GEKCO		−0.20	16.93		

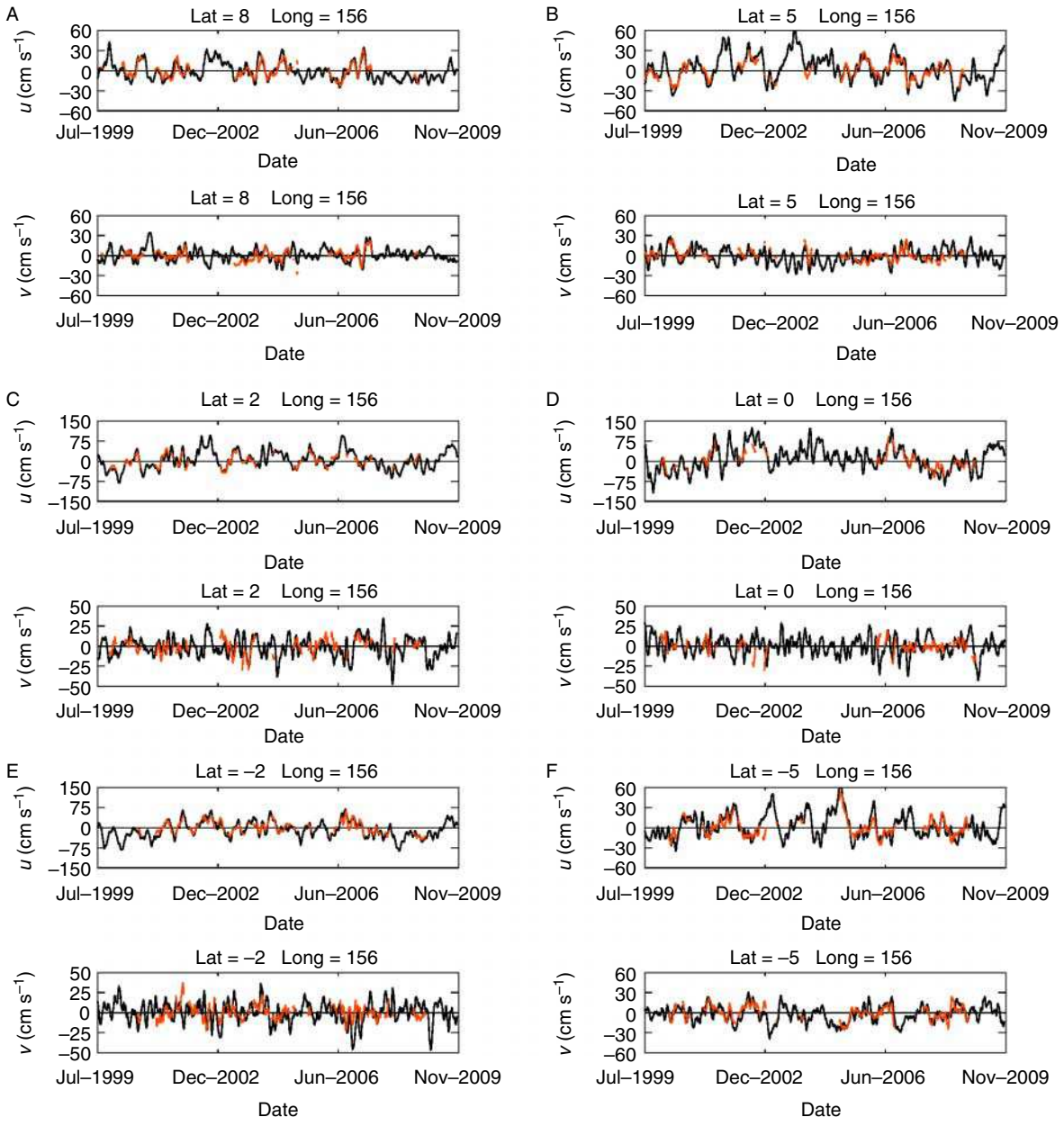

Fig. 4 Time series of the zonal (u, top) and meridional (v, bottom) components (in cm s^{-1}) along 156°E in the western Pacific Ocean as observed by ADCP moorings (red) and as estimated by GEKCO (black): A — (8°N, 156°E); B — (5°N, 156°E); C — (2°N, 156°E); D — (0°N, 156°E); E — (2°S, 156°E); and F — (5°S, 156°E). Note that the y-axis scales are different between the zonal and meridional components. Each time series was filtered at 30 days.

time series of current anomalies observed by current meter moorings corresponding to an Eulerian view of ocean dynamics. Unfortunately, time series are often interrupted by instrument failures or vandalism on the mooring lines, which prevents data recovery and produced gaps of ≥6 months. We considered only time series containing ≥3 full years of data in total. Note that each time series was normalized with its own mean value to focus only on the variability. Figs. 4 and 5 show the comparisons for the zonal and meridional components of moorings along 156°E (between 8°N and 5°S) and along the equator from 147°E to 110°W in the Pacific Ocean and 90°E in the Indian Ocean. Typical anomalies of the order of $O(1.0\,\mathrm{m\,s^{-1}})$ for the zonal

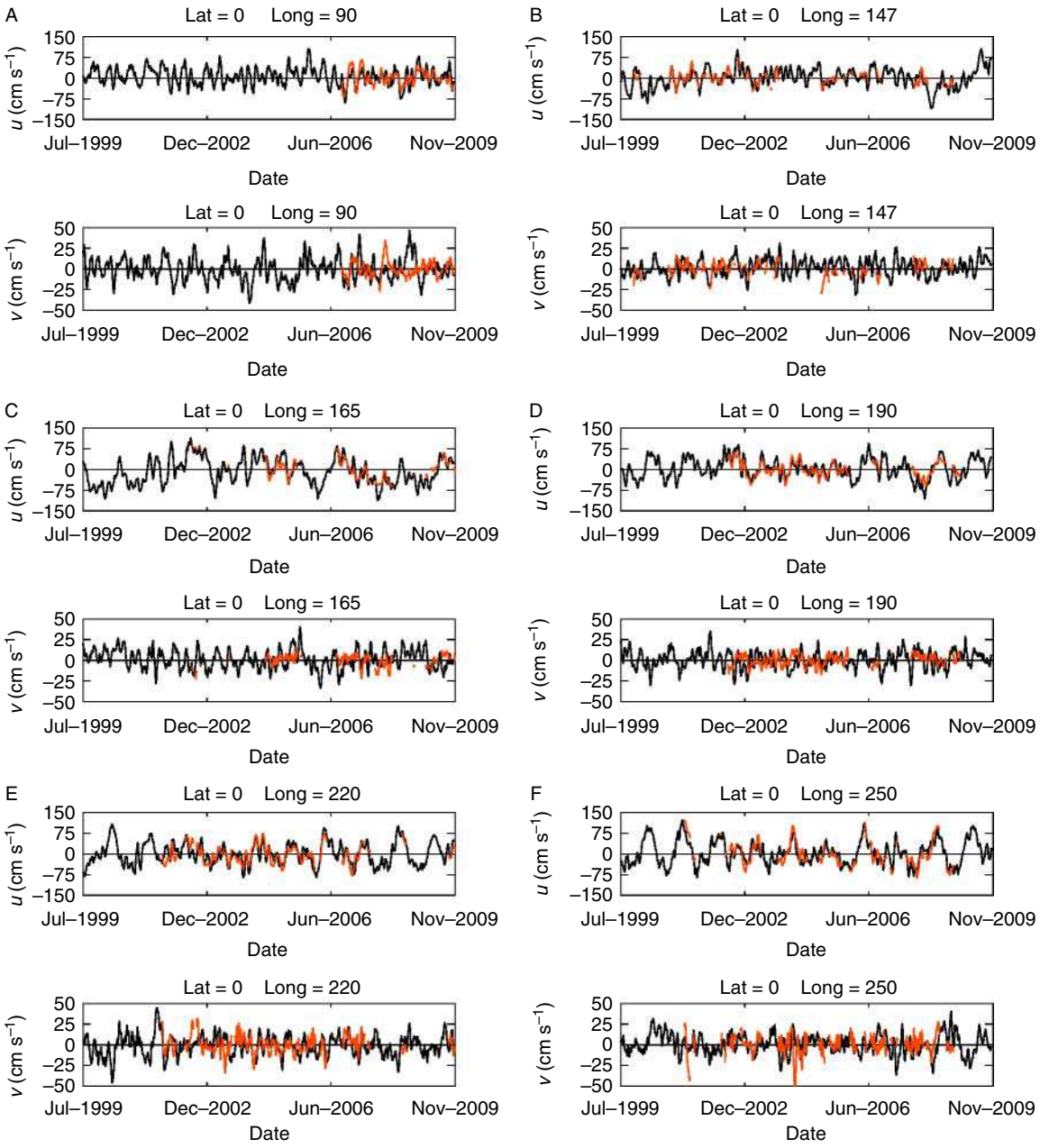

Fig. 5 Time series of the zonal (*u*, top) and meridional (*v*, bottom) components (in cm s^{-1}) for different equatorial positions (lat, long for each panel) along the Indian and Pacific oceans: A — (0°N, 90°E); B — (0°N, 147°E); C — (0°N, 165°E); D — (0°N, 190°E); E — (0°N, 220°E); and F — (0°N, 250°E). ADCP mooring indicated in red and GEKCO in black. Note that the *y*-axis scales are different between the zonal and the meridional components. Each time series was filtered at 30 days.

component were particularly well estimated by GEKCO, especially along the equator. For example, the time series at 165°E (Fig. 5C) exhibited positive anomalies between early 2001 and the end of 2007, which could be associated with zonal displacement of the warm pool toward the central Pacific with the development of the 2001–2002 El Niño event. Typical anomalies of $O(0.2\ m\ s^{-1})$ characterized the meridional component within the 2°N–2°S band with an amplitude ratio of 5 compared with the zonal one. The GEKCO estimate showed a similar ratio even if the correlations for most equatorial sites were not significant for the meridional component. Conversely,

Table 2 A — Comparisons for the zonal component (u) between the observed data by moored ADCP and the GEKCO model estimates along the equatorial Indian and Pacific oceans. N represents the number of collocated points to evaluate the mean, standard deviation (SD), root mean square difference (RMS diff), and correlation (ns = $p <$ 95% level of confidence). B — Same comparisons for the meridional component (v).

A						
	u	N	Mean	SD	RMS dif	Correlation
0°N–090°E	ADCP	1061	5.65	27.81	24.41	0.68
	GEKCO		10.73	31.65		
0°N–147°E	ADCP	1441	−2.60	20.99	33.17	0.66
	GEKCO		25.49	22.21		
0°N–165°E	ADCP	1117	−10.45	34.45	29.64	0.88
	GEKCO		10.48	43.44		
0°N–170°W	ADCP	1759	−26.26	26.45	22.70	0.81
	GEKCO		−34.75	35.90		
0°N–140°W	ADCP	1818	−13.95	32.86	40.02	0.76
	GEKCO		−47.72	35.01		
0°N–110°W	ADCP	1581	−18.11	45.15	40.95	0.83
	GEKCO		−50.56	35.10		
B						
	v	N	Mean	SD	RMS dif	Correlation
0°N–090°E	ADCP	1061	−2.25	9.24	19.48	ns
	GEKCO		5.94	14.16		
0°N–147°E	ADCP	1441	−3.17	7.82	17.67	ns
	GEKCO		10.56	8.76		
0°N–165°E	ADCP	1117	−5.08	6.84	13.10	ns
	GEKCO		−6.27	11.44		
0°N–170°W	ADCP	1759	−5.77	6.56	12.11	ns
	GEKCO		−5.69	10.03		
0°N–140°W	ADCP	1818	−3.18	10.06	14.60	0.26
	GEKCO		4.02	11.04		
0°N–110°W	ADCP	1581	4.22	11.73	16.82	ns
	GEKCO		10.20	12.31		

for the zonal component (Table 2), the correlations, ranging from 0.67 to 0.90, were significant for all sites (Table 3A). Away from the equator, the amplitudes of zonal and meridional currents were quite similar (Fig. 4), and correlations were significant for both components (Table 3).

[18] These ADCP data considered only a few locations in the tropics, leaving large parts of the global ocean unvalidated. Moreover, strictly speaking, the surface drifters were not completely independent from the present estimates. Instead, the estimates of currents derived from surface displacement of Argo floats were used as an independent data set. A total of 482,370 observations between 2000 and 2008 were considered with the global repartition by $5° \times 5°$ bins, as shown in Fig. 6A. The best coverage was found in the North Indian and North West Pacific oceans, whereas the Southern Ocean remains, not surprisingly, the least-sampled region. Because of the 10-day interval between each current estimate, we considered all data as independent estimates in each bin. The statistical significance level (at 95%) of the correlation ranges from 0.1 for well-documented bins ($N > 400$) to 0.2 ($N > 100$) for the least-sampled ones. Fig. 6 (B, C), shows the correlation between the estimated currents from Argo floats and GEKCO. Globally, statistics were significant for both zonal and meridional components, and higher values were obtained in many regions that were also characterized by high levels of kinetic energy (Fig. 3). Whereas a few bins were not significant for the zonal component, the lower values and the least significant bins were located along the equatorial band for the meridional com-

Table 3 A — Comparisons for the zonal component (u) between the observed data by moored ADCP and the GEKCO model estimates along 156°E. N represents the number of collocated points to evaluate the mean, standard deviation (SD), root mean square difference (RMS diff), and correlation ($p >$ 95% level of confidence). B — Same comparisons for the meridional component (v).

A						
	u	N	Mean	SD	RMS dif	Correlation
8°N–156°E	ADCP	1685	−4.47	10.86	11.92	0.86
	GEKCO		−14.47	12.75		
5°N–156°E	ADCP	1814	15.17	12.17	8.08	0.89
	GEKCO		11.13	15.25		
2°N–156°E	ADCP	1414	−7.88	21.41	15.64	0.90
	GEKCO		3.99	23.67		
0°N–156°E	ADCP	1102	−11.47	29.13	31.77	0.87
	GEKCO		11.96	41.55		
2°S–156°E	ADCP	1786	−8.92	21.86	27.76	0.90
	GEKCO		16.35	26.30		
5°S–156°E	ADCP	1870	−6.64	13.56	13.45	0.83
	GEKCO		2.70	17.24		
B						
	v	N	Mean	SD	RMS dif	Correlation
8°N–156°E	ADCP	1685	2.59	7.69	7.30	0.65
	GEKCO		4.20	9.15		
5°N–156°E	ADCP	1814	3.56	7.77	7.47	0.67
	GEKCO		3.22	9.95		
2°N–156°E	ADCP	1414	5.24	8.94	12.57	0.37
	GEKCO		11.13	10.79		
0°N–156°E	ADCP	1102	−3.48	8.26	14.40	ns
	GEKCO		−7.73	12.02		
2°S–156°E	ADCP	1786	−1.76	8.58	25.47	0.28
	GEKCO		−23.09	13.65		
5°S–156°E	ADCP	1870	−3.64	10.26	8.57	0.73
	GEKCO		−7.07	11.32		

ponent. This results from the estimates close to the equatorial singularity in the 5°-width bins in latitude. Averaged globally, the mean correlations were equal to 0.68 and 0.62 for the zonal and meridional component, respectively.

[19] As mentioned earlier, comparisons with independent data revealed noticeable differences in mean currents. We compared the mean values over the 2000–2008 period with the drifter data and a few sections in latitude of zonal current based on the ADCP data. We focused on the equatorial band where the currents were strong and characterized by fine meridional structures. All the fields exhibited similar westward and eastward currents both in amplitude and latitudinal width (Fig. 7). However differences as high as 20 cm s^{-1} were noted, and in some cases, one estimate deviated significantly from the others. As an example, a large structure of eastward current at 165°E between the equator and 7°N was observed in the GEKCO estimates, whereas the ridge between the South Equatorial Current and the North Equatorial Counter Current was expected (Fig. 7A). We diagnosed the presence of this structure in absolute dynamic topography from which the geostrophic zonal current was derived. Compared with the Pacific Ocean, the latitudinal structures in the Atlantic equatorial ocean were even finer and were consistent among the different estimates.

Discussion

[20] Satellites are the primary sources of observations for the GEKCO surface ocean currents, providing an

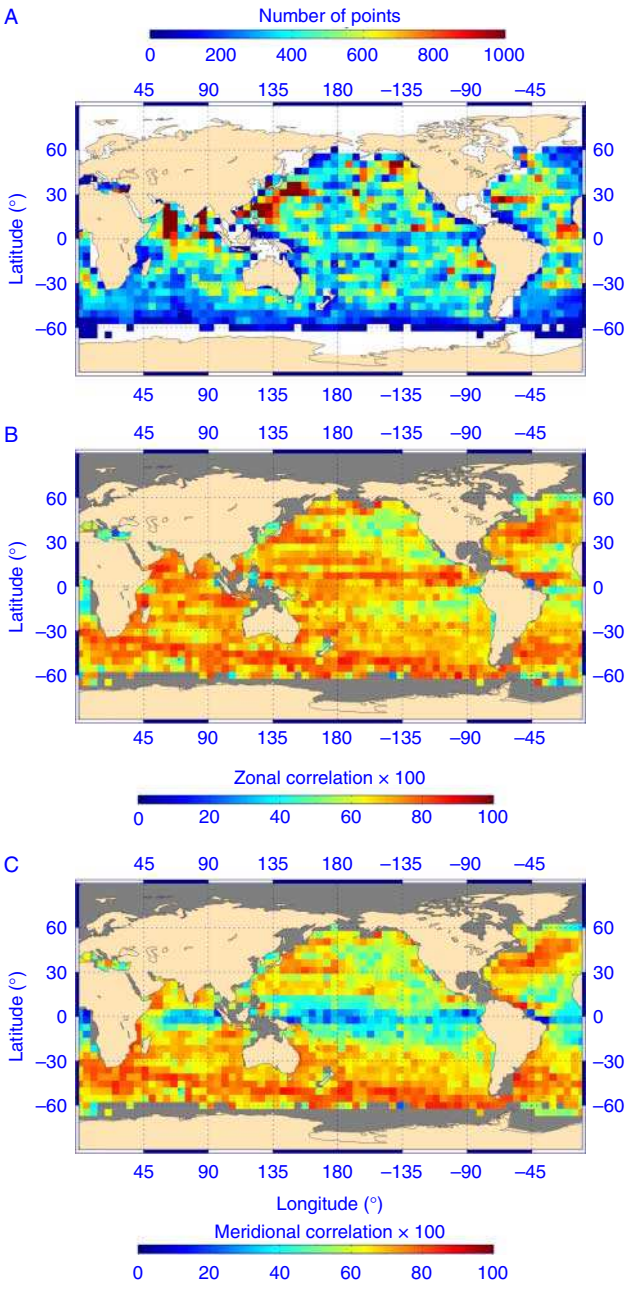

Fig. 6 A — Number of points by 5° × 5° bins used in the statistical comparison between the currents estimated by the Argo float displacement and GEKCO. B and C — Correlations for the zonal component (B) and the meridional component (C). Only correlations that were significant at the 95% level of confidence are plotted.

unprecedented spatiotemporal coverage at global scale over the last 20 years. The geostrophic component of the current is derived directly from the dynamic topography observed from space, whereas the wind-driven component is based on the conjoint use of wind stress and a physically based statistical model calibrated on 15-m drogued drifter data. The approach is essentially similar to the form proposed by Lagerloef et al. (1999) but differs in the present study by considering a time dependence of the (h_e, r_e) parameters (Eqs. 4a, 4b) implied in the Ekman motion instead of using constant values. Both approaches rely on accurate observations of current provided by the Global Drifter Program data developed since 1979 (Niiler and Paduan 1995; Lumpkin and Pazos 2007). Recently, Grodsky et al. (2011) reported a spurious temporal trend that has introduced errors in drifter currents. The origin of the problem was related to the contamination of the drogue-on data set by undrogued data, especially during the 2004–2008 period. The validation with independent data sets provides confidence about the reliability of the GEKCO estimates. As recommended by Grodsky et al. (2011), the use of drogue-on data could be achieved only by considering the first 90 days of data from each drifter. We choose to focus on the Indian Ocean because it represents a sector where data exhibit strong variations between the northern part that remains well sampled and the southern part where the total number of points for the comparison is much lower (Fig. 8A, B). The results are presented in terms of correlation between the currents (u, v) estimated by the drifters and GEKCO (Fig. 8C–F). In the North Indian Ocean, correlations were relatively unchanged or slightly better when using the 90-day drifter data; this result confirms the recommendations from Grodsky et al. (2011). In the South Indian Ocean, correlations were higher in most bins with the full data set, which suggests that the present determination has been only modestly affected by the bias in the full drifter data set. This latter point is reinforced by the averaged correlations over the entire Indian Ocean, which were not significantly different between the two data sets (0.79 vs. 0.77 and 0.77 vs. 0.75 between the full set and the 90-day set for the zonal and meridional component, respectively). This result suggests that the GEKCO estimates could be used in further studies to improve the drogue presence detection in the full drifter data set.

[21] The determination of GEKCO is based on the assumption that the near-surface velocity field can be decomposed into a geostrophic component and a wind-driven part. In the tropical Pacific, Ralph and

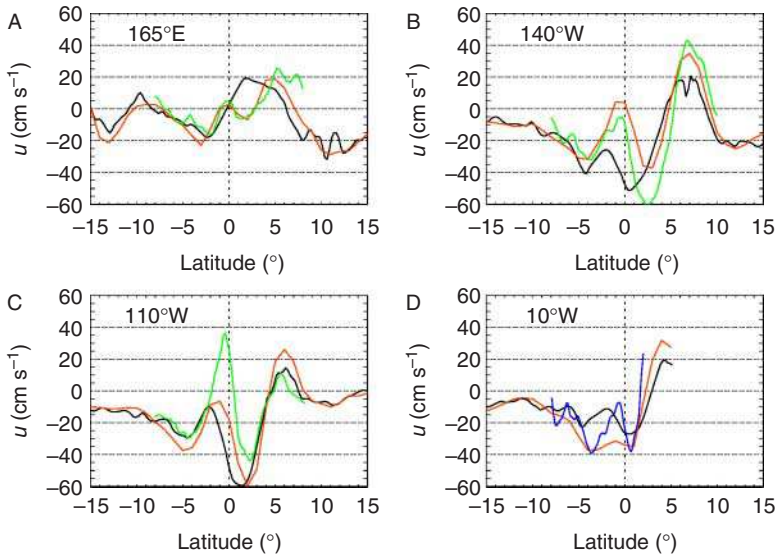

Fig. 7 Meridional sections of the mean zonal component (in cm s^{-1}) at 165°E, 140°W, 110°W, and 10°W for the drifter climatology (red) and the present estimates (in black). Additional estimates are given by Johnson et al. (2002) for the Pacific (green) and by Kolodziejczyk et al. (2009) for the Atlantic Ocean (blue).

Niiler (1999) reported that almost 80% of the variance of current measured by the drifter is accounted for by such a balance. Their results also support the observation that the strongest ageostrophic currents occurred in regions of the strongest winds. The strength of surface current also depends upon the turbulent processes that transport vertically the wind momentum, and several experiments confirm that the transport of water due to the winds is consistent with Ekman layer theories (Price et al. 1987; Chereskin and Roemmich 1991; Wijffels et al. 1994). Direct observations also show that the wind-driven transport is strongly surface trapped and that the long-term mean current exhibits a spiral-like structure. Consistent with such Ekman dynamics, we found that the deviation of the surface current at 15-m depth from the wind equals 52° ± 4° within the tropical Pacific Ocean. In comparison, Ralph and Niiler (1999) reported a deviation of 55° ± 5° by using a Ekman balance that specified the turbulent stress as a linear function of depth. The relative importance of each component in the present estimate of mean surface currents could be evaluated by considering a meridional section across the Atlantic Ocean (Fig. 9). Comparisons with drifter climatology (Lumpkin and Garraffo 2005) ensure that the present estimates along this section agree well with observational evidence. All across the basin, the total current results from a composition of geostrophic and wind-driven components with quite similar amplitudes, the dominance of the zonal wind-driven current being more important in the northern and southern subtropical regions where trade winds are established. For the meridional component, the balance is different and results in a more systematic compensation between the wind-driven and the geostrophic current. On each side of the equator, the wind-driven part exceeds the geostrophic component, resulting in a net deficit of water mass that is partially compensated by the vertical upwelling. Southward of 40°S, the positive meridional component could be associated with the northward Ekman flux in response to the strong and permanent westerly winds, whereas the eastward zonal current represents the signature of the ACC that encircles the Antarctic continent.

Biological Implications

[22] Compared with terrestrial environments, theoretical and predictive models of marine ecosystems that account for the complex food-web interactions also need to consider the fluid dynamics of oceanic environments. For example, the relationships among marine biota, biogeochemistry, and global climate are of utmost importance to determine the consequences of global change. In the ocean, the spatiotemporal distribution of phytoplankton and zooplankton populations results from changes in their environment generated by turbulent processes (Abraham 1998). Primary production is usually partitioned into the locally regenerated production and the new production resulting from mixing, stirring, and upwelling of nutrients into the euphotic zone (e.g., Dugdale and Goering 1967). The surface currents represent one key element to understand and describe these complex relationships. They are also needed for studies of top predators, the upper trophic level of the marine food web. Two examples illustrate such connectivities: horizontal surface stirring observed during iron

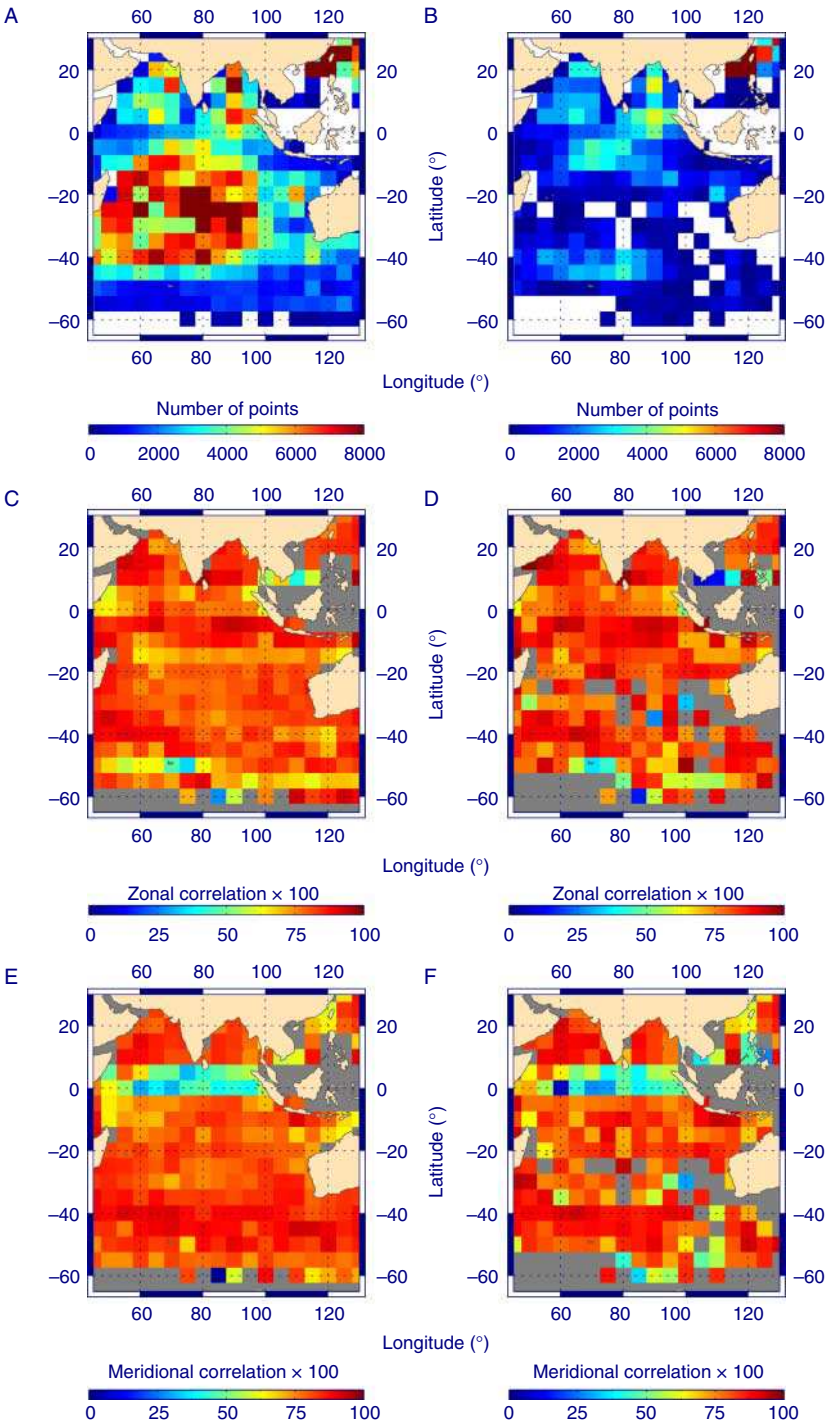

Fig. 8 Comparison between the total set of Lagrangian surface drifters (A, C, E) and the set of 90-day drifters data only (B, D, F) within the Indian Ocean representing number of points by 5° × 5° bins used in the statistical comparison between the currents estimated by the Argo float displacement and GEKCO (A and B), and correlations for the zonal component (C and D) and the meridional component (E and F). Only correlations that were significant at the 95% level of confidence are plotted.

fertilization experiments; and the deconvolution between the surface current and the observed displacements of animals.

[23] In the open ocean, remotely sensed ocean color images reveal the signature of phytoplankton blooms and provide evidence for their dispersal by horizontal stirring. In order to test John Martin's (1990) iron hypothesis, several mesoscale iron enrichment experiments have been conducted in different biogeochemical provinces (de Baar et al. 2005). During the Southern Ocean Iron Release Experiment (SOIREE), Abraham et al. (2000) and Boyd and Law (2001) argued that the ribbonlike bloom was produced from the enriched patch six weeks after the iron fertilization took place. They also proposed that stirring was the major process to control bloom development and phytoplankton mixing. Based on the estimate of surface currents, Lagrangian coherent structures (LCSs) can be determined to help the interpretation of the SOIREE observations. This can be done by estimating a direct measure of the local stirring through the computation of the finite-size Lyapunov exponent (FSLE). The FSLE represents the inverse time for which a couple of particles reach a prescribed spatial separation. When the time sequence is forward (backward), the computation of FSLE depicts LCSs associated with the convergence (divergence) of the flow. Typically, the initial distance is set to 0.025°, and the prescribed separation distance is set to 1°, in order to focus on mesoscale structures (d'Ovidio et al. 2004; Rossi et al. 2008).

[24] Currents and backward FSLE maps placed in the same time sequence

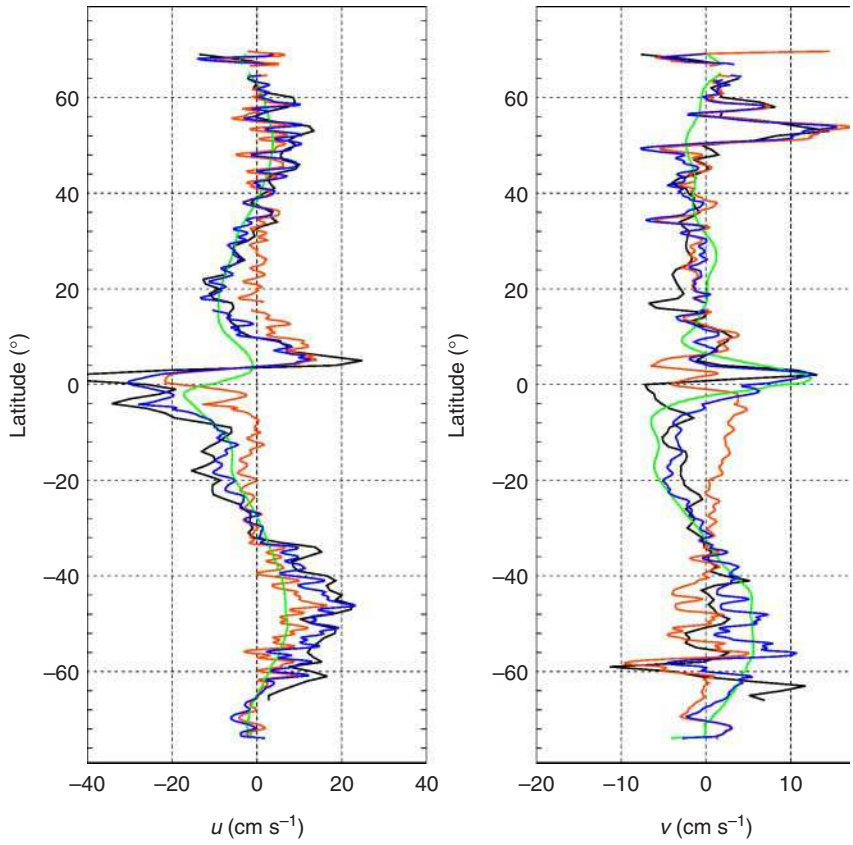

Fig. 9 Meridional section between 80°S and 80°N across the Atlantic Ocean along 23°W for the zonal (A) and meridional (B) components issued from the surface drifter climatology (black) given by Lumpkin and Garraffo (2005) and the total present current (blue), the latter resulting from the combination of the geostrophic (red) and wind-driven (green) components of GEKCO.

of the SOIREE images as shown by Abraham et al. (2000) are displayed in Fig. 10. The enlarged area centered around the SOIREE zone is characterized by a general eastward flow created by different currents of $\sim 30\,\mathrm{cm\,s^{-1}}$ and by a permanent presence of LCSs with high values of $\sim 0.2\,\mathrm{d^{-1}}$ corresponding to a 5-d time scale. Within the SOIREE area and near the released point of iron enrichment, backward FSLEs evolve from weak values ($< 0.01\,\mathrm{d^{-1}}$), corresponding to the absence of LCSs on 23 March 1999 (Fig. 10F). The FSLE diagnostics provide complementary elements to highlight the dynamic scenario of the SOIREE experiment. At the iron release, owing to the presence of a relatively deep mixed layer (Boyd and Law 2001) and the absence of LCSs in flow structure, the iron concentration remained high enough to allow the future development of the phytoplankton bloom. Then, associated with the ongoing appearance of the bloom, the flow was stirred by northward-propagating LCSs due to the intensification of the surface currents (Fig. 10F). Finally, we confirmed that the ribbonlike bloom as observed by chlorophyll satellite images (Abraham et al. 2000) represented the chlorophyll signature associated with the stirring of the LCSs. Fig. 10H shows that this LCS is deformed and advected northeastward by the mean flow close to the border of the SOIREE domain. Because the evolution of LCSs in a turbulent flow is by essence unpredictable, fertilization experiments should be considered with caution because adverse consequences remain possible (Neufeld et al. 2002).

[25] The use of satellites for precise localization (telemetry) combined with surface currents can be used to qualify the mechanical action of currents on the displacement of marine animals (Luschi et al. 2001; Girard et al. 2006). This approach aims to distinguish the tracking path (what the animal did) from the motor path (what the animal intended to do) to test homing ability (Luschi et al. 2007), to analyze in detail, for instance, a turtle's navigational performance (Benhamou et al. 2011) and to understand spatiotemporal foraging (Fossette et al. 2010). The interpretation of the behaviors and movements of individual animals requires that the trajectories of each displacement be examined from a Lagrangian perspective. Determining errors is rather difficult because of the heterogeneous and nonstationary regime of the flow. Nevertheless, in any particular region of the ocean, an estimate of such errors can be determined by considering the trajectory of an independent Lagrangian drifter. The displacement of any drifter in the ocean is due only to the motion. If we manage to compute a "current-corrected" track by using both the geostrophic and Ekman components, the only error on the drifter dis-

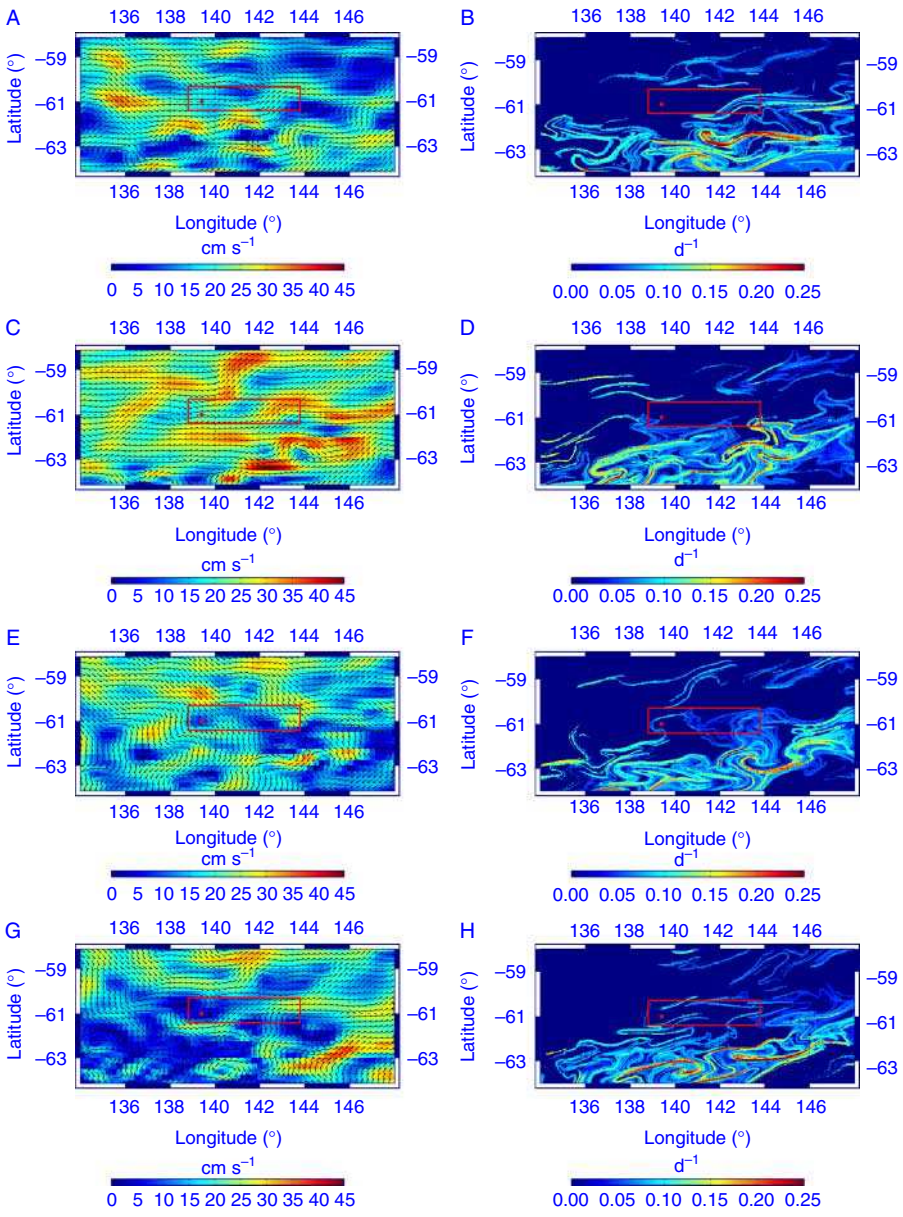

Fig. 10 Images of GEKCO (left) and FSLE (right) fields during the SOIREE experiment for 14 February 1999 (A and B), 10 March 1999 (C and D), 23 March 1999 (E and F), and 6 April 1999 (G and H). The red square indicates the area as shown in Abraham et al. (2000), where the red dot indicates the start of the SOIREE experiment on 9 February 1999.

placement will be due to errors in the currents. When dealing with marine animals, these errors will superimpose on the animals' motions.

[26] As an example, we estimated this correction for a drifter deployed in the northern part of the Mozambique Channel. Fig. 11 displays the original drifter trajectory (black curve), on which we superimposed the current-corrected tracks by using only geostrophy (blue curve) and geostrophy plus the Ekman component (red curve). We interpreted the differences between both current-corrected trajectories as a combination of errors resulting from the GEKCO estimate and of errors from physical small-scale processes that are inherently recorded in the trajectory of any individual drifter. Moreover, consideration of the wind-driven component reveals the importance of the wind influence on long-term displacements. If our GEKCO estimates were perfect representations of the oceanic total currents, the red curve should not move from the initial release point. This methodology also has biological implications. Typically, when applied to green turtle displacement, this correction provided information on ground-related movement compared with water-mass–related movement (Girard et al. 2006; Benhamou et al. 2011). In such cases, better current estimates will provide an improved assessment of the mechanical impact of ocean currents on turtle behavior. For studies integrating spatial analysis of the movement of marine animals, we recommend the systematic deployment of additional drifters when the animals are tagged and then released. Such types of studies are crucial for the long-term monitoring of migratory populations and for the management of efforts needed for future restoration (Myers and Worm 2003).

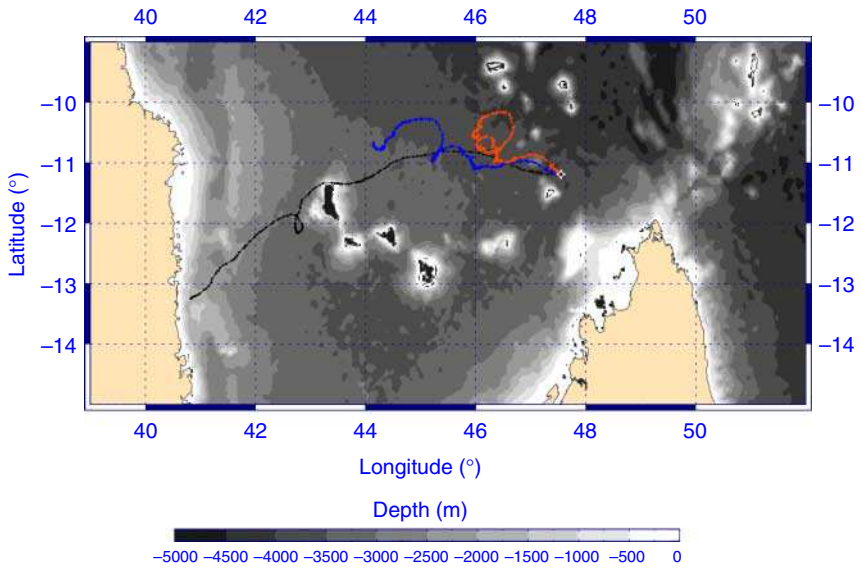

Fig. 11 Trajectory of a Lagrangian surface drifter at the entrance of the Mozambique Channel between 1 and 13 April 2008 (black line; dots mark the 293 hourly positions). The blue line shows the "corrected trajectory" by the geostrophic component, and the red line shows the corrections by the geostrophic and wind-driven currents. The white star marks the released point of the drifter. The background field represents the bottom topography.

Significance to Aquatic Environments

[27] A fundamental goal of physical oceanography is to provide a first-order description of the global ocean circulation. Such information can be used to model ocean currents and thus understand the displacement of matter, ranging from marine algae to turtles, and from plastic debris to oil spills. This study used the GEKCO model, which includes both geostrophic and Ekman current components of oceanic currents from remote-sensing altimeter and scatterometer data sets, to provide a global survey of the major ocean currents rather than a detailed description of the different regional surface circulations. The GEKCO estimates facilitated the evaluation of ocean surface velocity at a spatial resolution of 0.25° (~28 km) from 82°N to 82°S, retrospectively to October 1992. The estimates were validated against different data sets, and examples of applications to a diverse set of scientific problems were provided in which an improved understanding of ocean currents was required. GEKCO was able to model the relationships between ocean currents and phytoplankton blooms during the SOIREE iron fertilization experiment, which in this case were related to mass transport via Lagrangian coherent structures. GEKCO also enabled the separation of ground-related movements from water-mass–related movements of the displacement of marine turtles. In such cases, caution must be used in the interpretation of the difference of these two movements because of cumulative effects of different error sources.

Acknowledgments We are sincerely grateful to the different data providers, mainly including the CERSAT and the CNES/AVISO teams, the Global Drifter Program, the TAO/TRITON, PIRATA, and RAMA arrays, the Joint Archive for Shipboard ADCP, and the ARGO surface current estimates by J. Xie and J. Zhu. Improvements and comments provided by the two anonymous reviewers as well as editors Dr. André Visser and Dr. Joe Ackerman are greatly appreciated. Special thanks go to Mayra Pazos and staff at AOML for their work on drifters, to Dr. Cristóbal López and Dr. Emilio Hernández-García for providing their code for the FSLE computation, and to Dr. Simon Benhamou and Dr. Phil Wallhead for their careful critical reading.

References

Abraham, E. R. 1998. The generation of plankton patchiness by turbulent stirring. Nature **391**: 577–580, doi:10.1038/35361.

Abraham, E. R., C. S. Law, P. W. Boyd, S. J. Lavender, M. T. Maldonado, and A. R. Bowie. 2000. Importance of stirring in the development of an iron-fertilized phytoplankton bloom. Nature **407**: 727–730, doi:10.1038/35037555.

Benhamou, S., J. Sudre, J. Bourjea, S. Ciccione, A. De Santis, and P. Luschi. 2011. The role of geomagnetic cues in green turtle open sea navigation. PLoS ONE **6**: e26672, doi:10.1371/journal.pone.0026672.

Boyd, P. W., and C. S. Law. 2001. The Southern Ocean Iron Release Experiment (SOIREE)—introduction and summary. Deep Sea Res. Part II Top. Stud. Oceanogr. **48**: 2425–2438, doi:10.1016/S0967-0645(01)00002-9.

Chelton, D. B., M. G. Schlax, and R. M. Samelson. 2011. Global observations of nonlinear mesoscale eddies. Prog. Oceanogr. **91**: 167–216, doi:10.1016/j.pocean.2011.01.002.

Chereskin, T. K., and D. Roemmich. 1991. A comparison of measured and wind-derived Ekman transport at 11°N in the Atlantic

Ocean. J. Phys. Oceanogr. **21**: 869–878, doi:10.1175/1520-0485(1991)021<0869:ACOMAW>2.0.CO;2.

de Baar, H. J. W., et al. 2005. Synthesis of iron fertilization experiments: From the Iron Age in the Age of Enlightenment. J. Geophys. Res. **110** (C9): C09S16, doi:10.1029/2004JC002601.

Dohan, K., and N. Maximenko. 2010. Monitoring ocean currents with satellite sensors. Oceanography **23**: 94–103, doi:10.5670/oceanog.2010.08.

d'Ovidio, F., V. Fernández, E. Hernández-García, and C. López. 2004. Mixing structures in the Mediterranean Sea from finite-size Lyapunov exponents. Geophys. Res. Lett. **31**: L17203, doi:10.1029/2004GL020328.

Dugdale, R. C., and J. J. Goering. 1967. Uptake of new and regenerated forms of nitrogen in primary productivity. Limnol. Oceanogr. **12**: 196–206, doi:10.4319/lo.1967.12.2.0196.

Fossette, S., V. J. Hobson, C. Girard, B. Calmettes, P. Gaspar, J.-Y. Georges, and G. C. Hays. 2010. Spatio-temporal foraging patterns of a giant zooplanktivore, the leatherback turtle. J. Mar. Syst. **81**: 225–234, doi:10.1016/j.jmarsys.2009.12.002.

Garçon, V. C., A. Oschlies, S. C. Doney, D. McGillicuddy, and J. Waniek. 2001. The role of mesoscale variability on plankton dynamics in the North Atlantic. Deep Sea Res. Part II Top. Stud. Oceanogr. **48**: 2199–2226, doi:10.1016/S0967-0645(00)00183-1.

Girard, C., J. Sudre, S. Benhamou, D. Roos, and P. Luschi. 2006. Homing in green turtles *Chelonia mydas*: Oceanic currents act as a constraint rather than as an information source. Mar. Ecol. Prog. Ser. **322**: 281–289, doi:10.3354/meps322281.

Grodsky, S. A., R. Lumpkin, and J. A. Carton. 2011. Spurious trends in global surface drifter currents. Geophys. Res. Lett. **38**: L10606, doi:10.1029/2011GL047393.

Hummon, J. M., and E. Firing. 2003. A direct comparison of two RDI shipboard ADCPs: A 75-kHz ocean surveyor and a 150-kHz narrow band. J. Atmos. Ocean. Technol. **20**: 872–888, doi:10.1175/1520-0426(2003)020<0872:ADCOTR>2.0.CO;2.

Johnson, E. S., F. Bonjean, G. S. E. Lagerloef, J. T. Gunn, and G. T. Mitchum. 2007. Validation and error analysis of OSCAR sea surface currents. J. Atmos. Oceanic Technol. **24**: 688–701, doi:10.1175/JTECH1971.1.

Johnson, G. C. 2001. The Pacific Ocean subtropical cell surface limb. Geophys. Res. Lett. **28**: 1771–1774, doi:10.1029/2000GL012723.

Johnson, G. C., B. M. Sloyan, W. S. Kessler, and K. E. McTaggart. 2002. Direct measurements of upper ocean currents and water properties across the tropical Pacific during the 1990s. Prog. Oceanogr. **52**: 31–61, doi:10.1016/S0079-6611(02)00021-6.

Kolodziejczyk, N., B. Bourlès, F. Marin, J. Grelet, and R. Chuchla. 2009. Seasonal variability of the Equatorial Undercurrent at 10°W as inferred from recent in situ observations. J. Geophys. Res. **114** (C6): C06014, doi:10.1029/2008JC004976.

Lagerloef, G. S. E., R. Lukas, F. Bonjean, J. T. Gunn, G. T. Mitchum, M. Bourassa, and A. J. Busalacchi. 2003. El Niño tropical Pacific Ocean surface current and temperature evolution in 2002 and outlook for early 2003. Geophys. Res. Lett. **30**: 1514–1518, doi:10.1029/2003GL017096.

Lagerloef, G. S. E., G. T. Mitchum, R. B. Lukas, and P. P. Niiler. 1999. Tropical Pacific near-surface currents estimated from altimeter, wind, and drifter data. J. Geophys. Res. **104** (C10): 23313–23326, doi:10.1029/1999JC900197.

Llido, J., V. Garçon, J. R. E. Lutjeharms, and J. Sudre. 2005. Event-scale blooms drive enhanced primary productivity at the Subtropical Convergence. Geophys. Res. Lett. **32**: L15611, doi:10.1029/2005GL022880.

Lumpkin, R., and Z. Garraffo. 2005. Evaluating the decomposition of tropical Atlantic drifter observations. J. Atmos. Ocean. Technol. **22**: 1403–1415, doi:10.1175/JTECH1793.1.

Lumpkin, R., and M. Pazos. 2007. Measuring surface currents with Surface Velocity Program drifters: The instrument, its data and some recent results. Pp. 39–67. *In* A. Griffa, A. D. Kirwan, A. J. Mariano, T. Ozgokmen, and T. Rossby [eds.], Lagrangian Analysis and Prediction of Coastal and Ocean Dynamics (LAPCOD). Cambridge University Press, doi:10.1017/CBO9780511535901.003.

Luschi, P., S. Akesson, A. Broderick, F. Glen, B. Godley, F. Papi, and G. Hays. 2001. Testing the navigational abilities of ocean migrants: Displacement experiments on green sea turtles (*Chelonia mydas*). Behav. Ecol. Sociobiol. **50**: 528–534, doi:10.1007/s002650100396.

Luschi, P., S. Benhamou, C. Girard, S. Ciccione, D. Roos, J. Sudre, and S. Benvenuti. 2007. Marine turtles use geomagnetic cues during open-sea homing. Curr. Biol. **17**: 126–133, doi:10.1016/j.cub.2006.11.062.

Maes, C., K. Ando, T. Delcroix, W. S. Kessler, M. J. McPhaden, and D. Roemmich. 2006. Observed correlation of surface salinity, temperature and barrier layer at the eastern edge of the western Pacific warm pool. Geophys. Res. Lett. **33**: L06601, doi:10.1029/2005GL024772.

Maes, C., J. Sudre, and V. Garçon. 2010. Detection of the eastern edge of the equatorial Pacific warm pool using satellite-based ocean color observations. Sci. Online Lett. Atmos. **6**: 129–132, doi:10.2151/sola.2010-033.

Martin, J. H. 1990. Glacial-interglacial CO_2 change: The iron hypothesis. Paleoceanography. **5**: 1–13, doi:10.1029/PA005i001p00001.

Moore, D. W. H., and S. G. Philander. 1978. Modeling of the tropical oceanic circulation. Pp. 319–361. *In* E. D. Goldberg [ed.], The Sea. Wiley-Interscience.

Myers, R. A., and B. Worm. 2003. Rapid worldwide depletion of predatory fish communities. Nature **423**: 280–283, doi:10.1038/nature01610.

Neufeld, Z., P. H. Haynes, V. Garçon, and J. Sudre. 2002. Ocean fertilization experiments may initiate a large scale phytoplank-

ton bloom. Geophys. Res. Lett. **29**: 1534–1538, doi:10.1029/2001GL013677.

Niiler, P. P., N. A. Maximenko, and J. C. McWilliams. 2003. Dynamically balanced absolute sea level of the global ocean derived from near-surface velocity observations. Geophys. Res. Lett. **30**: 2164–2168, doi:10.1029/2003GL018628.

Niiler, P. P., and J. D. Paduan. 1995. Wind-driven motions in the Northeast Pacific as measured by Lagrangian drifters. J. Phys. Oceanogr. **25**: 2819–2830, doi:10.1175/1520-0485(1995)025<2819:WDMITN>2.0.CO;2.

Picaut, J., M. Ioualalen, C. Menkes, T. Delcroix, and M. J. McPhaden. 1996. Mechanism of the zonal displacements of the Pacific warm pool: Implications for ENSO. Science **274**: 1486–1489, doi:10.1126/science.274.5292.1486.

Picaut, J., and R. Tournier. 1991. Monitoring the 1979–1985 equatorial Pacific current transports with expendable bathythermograph data. J. Geophys. Res. **96** (Suppl.): 3263–3277.

Price, J. F., R. A. Weller, and R. R. Schudlich. 1987. Wind-driven ocean currents and Ekman transport. Science **238**: 1534–1538, doi:10.1126/science.238.4833.1534.

Ralph, E. A., and P. P. Niiler. 1999. Wind-driven currents in the tropical Pacific. J. Phys. Oceanogr. **29**: 2121–2129, doi:10.1175/1520-0485(1999)029<2121:WDCITT>2.0.CO;2.

Richardson, P. L. 1989. Worldwide ship drift distributions identify missing data. J. Geophys. Res. **94** (C5): 6169–6176, doi:10.1029/JC094iC05p06169.

Robel, A. A., M. S. Lozier, S. F. Gary, G. L. Shillinger, H. Bailey, and S. J. Bograd. 2011. Projecting uncertainty onto marine megafauna trajectories. Deep Sea Res. Part I Oceanogr. Res. Pap. **58**: 915–921, doi:10.1016/j.dsr.2011.06.009.

Rossi, V., C. López, J. Sudre, E. Hernández-García, and V. Garçon. 2008. Comparative study of mixing and biological activity of the Benguela and Canary upwelling systems. Geophys. Res. Lett. **35**: L11602, doi:10.1029/2008GL033610.

Sudre, J., and R. Morrow. 2008. Global surface currents: A high-resolution product for investigating ocean dynamics. Ocean Dyn. **58**: 101–118, doi:10.1007/s10236-008-0134-9.

Tew Kai, E., V. Rossi, J. Sudre, H. Weimerskirch, C. Lopez, E. Hernandez-Garcia, F. Marsac, and V. Garçon. 2009. Top marine predators track Lagrangian coherent structures. Proc. Natl. Acad. Sci. USA. **106**: 8245–8250, doi:10.1073/pnas.0811034106.

van Meurs, P., and P. P. Niiler. 1997. Temporal variability of the large-scale geostrophic surface velocity in the northeast Pacific. J. Phys. Oceanogr. **27**: 2288–2297, doi:10.1175/1520-0485(1997)027<2288:TVOTLS>2.0.CO;2.

Wijffels, S., E. Firing, and H. Bryden. 1994. Direct observations of the Ekman balance at 10°N in the Pacific. J. Phys. Oceanogr. **24**: 1666–1679, doi:10.1175/1520-0485(1994)024<1666:DOOTEB>2.0.CO;2.

Xie, J., and J. Zhu. 2008. Estimation of the surface and mid-depth currents from Argo floats in the Pacific and error analysis. J. Mar. Syst. **73**: 61–75, doi:10.1016/j.jmarsys.2007.09.001.

Xie, J., and J. Zhu. 2009. A dataset of global ocean surface currents for 1999–2007 derived from Argo float trajectories: Comparison with surface drifter and TAO measurements. Atmos. Oceanol. Sci. Lett. **2**: 97–102.

Received: 24 February 2012
Amended: 28 June 2012
Accepted: 20 October 2012